ORIGINAL RESEARCH ARTICLE

Graphene-Based Metamaterial Absorber with Perfect Multi-band Absorption

Yingming Song[1] · Xin-Hua Deng[1,2,3] · Pingsheng Zhang[1] · Fumin Guo[1] · Kaipeng Qin[1]

Abstract

In this paper, we propose an absorber with adjustable single-layer graphene multi-band perfect absorption, which has the advantages of simple structure, polarization insensitivity, tunability, multi-band absorption, and high sensitivity. The device can achieve four perfect absorption peaks at the same time, and the absorption rate of all absorption peaks is above 99%. The absorption effect of the absorber can be efficiently adjusted and controlled by adjusting the geometric parameters of the single-layer graphene array and the thickness of the dielectric layer. In addition, by changing the strength of the applied magnetic field, the Fermi level, and the relaxation rate of graphene, the absorption of the device can be dynamically adjusted, and high absorption can be maintained in the range of 0°–70° wide incidence angle. Finally, considering the potential sensing applications of the device, we measured maximum sensitivity (S) of 3.06 THz/RIU and a maximum figure of merit (FOM) of 54.6 when exposed to different ambient refractive indices, suggesting that the device can be used as a refractive index sensor. These results show that this study provides a new idea for the design of the tunable multi-band perfect metamaterial absorber based on graphene, which has great application value in many fields and provides a new reference for future research.

Keywords Graphene · metamaterial absorber · multi-band · terahertz · polarization insensitivity

Introduction

Metamaterials are a recently emerging type of artificial electromagnetic materials.[1–3] Because of their unique sub-wavelength structure, they exhibit many unnatural phenomena, such as negative refractive index,[4–6] perfect absorption,[7–9] and electromagnetic transparency.[10,11] At present, related metamaterial devices such as optical switches,[12] modulators, and filters[13–16] have been developed and widely used in the fields of terahertz (THz), infrared, and visible bands, providing many possibilities for light control. Metamaterial absorbers (MAs) are one of the most important applications of metamaterials. Because of their simple structure,

✉ Xin-Hua Deng
   dengxinhua@ncu.edu.cn

1   Department of Physics, Nanchang University, Nanchang 330031, People's Republic of China

2   State Key Laboratory of Advanced Technology for Materials Synthesis and Processing, Wuhan University of Technology, Wuhan 430070, People's Republic of China

3   State Key Laboratory of Millimeter Waves, Southeast University, Nanjing 210096, People's Republic of China

convenient design, and extremely thin thickness, they have greater application prospects than traditional absorbers. In 2008, Landy et al.[17] designed the structure of an MA which could produce effective electromagnetic resonance with incident electromagnetic waves in the THz radiation frequency range, and could achieve nearly 100% perfect absorption in a specific frequency range. However, given that metamaterial devices are designed to obtain ideal absorption effects, they will be designed with a unique structure.[18–20] Once the device is manufactured, the structural parameters are difficult to change, so the spectral effect and effect are fixed. Therefore, MAs with greater flexibility and tunability have broader application prospects. Thus, we need to add some special materials that can control their electromagnetic properties by stimulating external factors.

Since Novoselov and Geim[21] first prepared single-layer two-dimensional graphene flakes in 2004, researchers have found that graphene can replace traditional metal materials because of its excellent properties such as surface conductivity[22] and high carrier mobility.[23] This allows it to be used as a good platform for metamaterials and surface plasmons, which can exhibit strong constraints, unlike traditional surface plasmas such as gold and copper.[24]

In addition, the dynamic adjustability of graphene is an advantage for designing MAs.[25] The surface conductivity of graphene is determined by the Fermi level, so we can adjust the Fermi level by applying a gate voltage and regulating the magnetic field and photoexcitation, and indirectly control the conductivity and permittivity of graphene.[26,27] Consequently, graphene shines in the design of microwave metamaterials at THz bands and is widely used. For example, in 2019, Luo et al. proposed a dual-band polarization-insensitive perfect absorber that was tunable in the mid-infrared band, and obtained polarization-insensitive dual-band ideal absorption peaks at 9611 nm and 9924 nm, respectively.[28] In 2021, Yin et al.[29] proposed a three-dimensional dual-band perfect absorber that achieves absorption efficiencies of 99% and 97% at 1.125 THz and 1.1626 THz, respectively. In 2022, Chen et al.[18] proposed a multi-band MA based on dart-type single-layer graphene, which has the advantages of multi-band, polarization independence, and tunability. Many studies[30–33] have achieved good results, but these studies only focus on single-band or double-narrowband MAs, while multi-band absorbers are relatively rare, and the structure of current multi-band MAs is relatively complex due to stringent restrictions.

In this paper, we propose a multi-band perfect absorber based on single-layer graphene, which achieves multi-band perfect absorption at $f_I = 6.46$ THz, $f_{II} = 7.49$ THz, $f_{III} = 8.53$ THz, and $f_{IV} = 9.45$ THz with absorption rates of 99.68%, 99.60%, 99.87%, and 99.00%. Through the equivalent circuit model (ECM) and electric field distribution, the physical mechanism of perfect absorption is discussed. We then achieved dynamic tunability of the peak absorption spectrum and resonance frequency by adjusting the strength of the applied magnetic field, the Fermi level, and the relaxation rate of graphene. In addition, the influence of the geometric parameters of graphene and the structural parameters of the absorption band absorber is investigated. Finally, due to the symmetry of the geometry, we also explored that the absorber still has excellent absorption performance in a wide range of incidence angles. Finally, we investigated its sensing performance, with a maximum S and FOM of 3.06 THz/RIU and 54.6. In summary, the proposed structure has many potential advantages based on achieving perfect absorption in multiple bands. Compared with Liu et al.,[34] the proposed structure can generate more absorption peaks, with four absorption peaks greater than 99% at the same time. Compared with Zamzam et al.,[35] our proposed structure can maintain excellent absorption over a wider range of angle of incidence; even when the angle of incident light is 60°, the absorber can achieve an absorption rate of more than 90%. Compared with Cai et al.,[36] the proposed structure is simpler and easier to manufacture, and our proposed structure can adjust the absorptivity of multiple absorption peaks with absorptivity greater than 99%.

Design and Method

The monolayer graphene-based MA proposed in this paper consists of three layers, as shown in Fig. 1a. At the top is an array of graphene patterns, consisting of a hollow "*X*" pattern and four isosceles right triangles. The middle layer is a silicon dioxide (SiO$_2$) dielectric layer, and the bottom layer is gold (Au), forming a "sandwich" structure. During the simulation, the incident wave propagates vertically downward to the structural surface of the absorber, forming a multimode surface plasmon resonance. The relative permittivity of SiO$_2$ is 3.9, and the relative permittivity function of the gold layer is represented by the Drude model[37,38]:

$$\varepsilon_{\text{gold}} = 1 - \frac{\omega_p^2}{\omega(\omega + i\gamma)} \tag{1}$$

In this equation, ω is the angular frequency of the incident light, $\omega_p = 1.37 \times 10^6$ rad/s is the plasma oscillation frequency, and the electron collision frequency $\gamma = 1.21 \times 10^{14}$ rad/s. Figure 1b shows a side view of the structure, showing the thickness of each layer of the absorber. The SiO$_2$ layer thickness is $h_1 = 4.0$ μm. The thickness of the Au layer is $h_2 = 0.5$ μm, and the structure period $P = 4$ μm. Figure 1c is a top view of a periodic monolayer graphene array, showing the detailed parameters of the pattern. The width of the "*X*" pattern is $x_1 = 0.3$ μm, and the length of one side is $x_2 = 2.4$ μm.
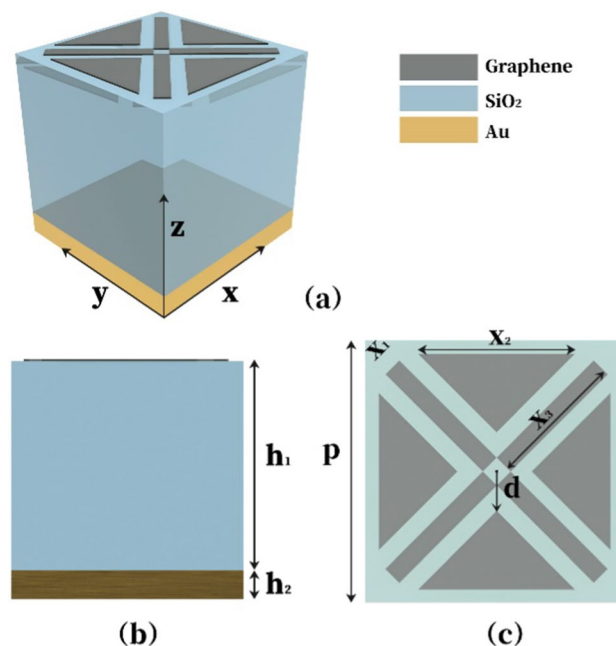
Fig. 1 (a) A three-dimensional view of the overall structure of the MA. (b) A side view of the MA. (c) Top view of graphene deposited on a SiO$_2$/Au substrate.

The length of the base side of the isosceles right triangle is $x_3 = 2.4\ \mu m$. The distance between the triangle and the center of the X pattern is $d = 0.6\ \mu m$.

We used the finite element method (COMSOL) for the simulation, set the period boundary conditions on the x- and y-axes, set the perfectly matched layers along the z-axis, and selected the appropriate mesh size to obtain excellent convergence results. So we can reflect the parameter S_{11} and transmit parameter S_{21}. Since the thickness of the Au layer is much greater than its skin depth, the incident wave is almost completely reflected, which results in a transmittance $T = |S_{21}|^2 \approx 0$. Therefore, the absorption rate can be expressed as[39]

$$A = 1 - R - T = 1 - R = 1 - |S_{11}|^2 \qquad (2)$$

Furthermore, the appropriate size of the grid has been selected for excellent convergence. Since graphene has a gap-free electronic band structure and single atomic thickness, it can be used as a two-dimensional material to improve computational efficiency, and the surface conductivity is generally characterized by the Kubo formula[32]:

$$\sigma(\omega) = \sigma(\omega)_{inter} + \sigma(\omega)_{intra}$$
$$= \frac{2e^2 k_B T}{\pi \hbar^2} \frac{i}{\omega + i/\tau} \ln\left[2\cosh\left(\frac{E_f}{2k_B T}\right)\right]$$
$$+ \frac{e^2}{4\hbar^2}\left[\frac{1}{2} + \frac{1}{\pi}\arctan\left(\frac{\hbar\omega - 2E_f}{2k_B T}\right)\right.$$
$$\left. - \frac{i}{2\pi}\ln\frac{\left(\hbar\omega + 2E_f\right)^2}{\left(\hbar\omega - 2E_f\right)^2 + 4\left(k_B T\right)^2}\right] \qquad (3)$$

In the formula, e is the electron charge, k_B is the Boltzmann constant, $T = 300$ K is the ambient temperature, $\hbar$ is the Planck constant, ω is the angular frequency of the incident wave, and E_f and τ are the Fermi level and relaxation rate, respectively. Depending on the modulation structural parameters, it is found that the absorption effect is best when $E_f = 1.0$ eV and $\tau = 0.9$ ps. It is worth noting here that k_B is the Boltzmann constant, and in the infrared band according to the principle of Pauli incompatibility, because k_B is much smaller than E_f in the THz band, σ_{inter} can be ignored. So the conductivity formula of graphene can be expressed as[40]

$$\sigma_g = \frac{ie^2 E_f}{\pi\hbar^2\left(\omega + i\tau^{-1}\right)} \qquad (4)$$

According to the above equation, we can know that the conductivity of graphene depends on the Fermi level and relaxation rate, so we can achieve dynamic adjustment by adjusting the Fermi level and relaxation rate without changing the structural parameters of the absorbing device.

In practical experiments,[41] a gold layer and a silica dielectric layer can be deposited on a silicon substrate by electron beam evaporation, and then a graphene layer can be grown on a copper catalyst by chemical vapor deposition. Then the "X" and isosceles triangle patterns were engraved by electron beam lithography and oxygen plasma etching to prepare a perfect absorber of single-layer graphene.

Results and Discussion

Figure 2 shows the absorption spectrum of a graphene-based multi-band MA designed by us. As a result, the absorber achieves multi-band perfect absorption at $f_I = 6.46$ THz, $f_{II} = 7.49$ THz, $f_{III} = 8.53$ THz, and $f_{IV} = 9.45$ THz, and the absorption rate reaches 99.68%, 99.60%, 99.87%, and 99.00%, corresponding to mode I, mode II, mode III, and mode IV. When the electromagnetic wave is incident perpendicular to the structure, the graphene on the surface is excited to produce a surface plasma, and the incident electromagnetic wave is consistent with the free electron frequency on the surface of the graphene, resulting in the phenomenon of surface plasmon resonance.[42] The incident electromagnetic wave energy is used to excite plasma oscillations, and the energy is strongly absorbed, thus achieving perfect absorption.

As shown in Fig. 3, the operation mechanism of the device can be illustrated using ECM. The graphene pattern on the surface is represented by three RLC circuits connected in series, which are arranged in parallel in the circuit. One represents the cross pattern, and the other two
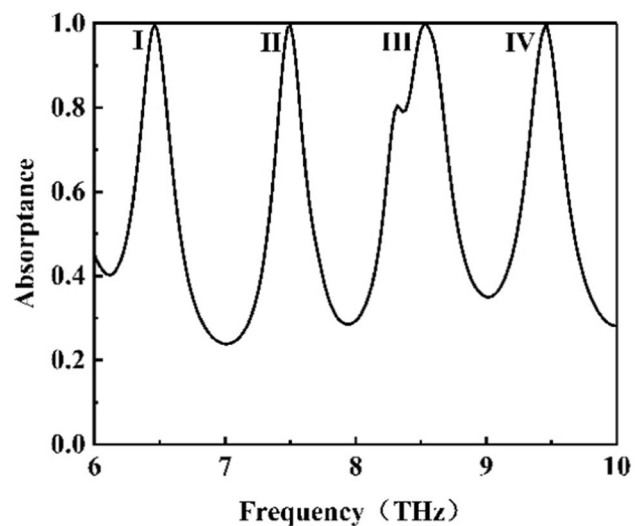

Fig. 2 The absorption spectrum of the designed MA.

represent the remaining four triangles. Resistors R_1, R_2, and R_3 are related to the loss of the structure, with L_1, L_2, and L_3 representing the inductance of the graphene pattern, and C_1, C_2, and C_3 representing the electrical coupling between the graphene pattern and the metal ground.[43]

The reflection coefficient of a device can be expressed as

$$S_{11} = \frac{Z_{in} - Z_0}{Z_{in} + Z_0} \tag{5}$$

where Z_{in} and Z_0 refer to the input impedance of MA and the intrinsic impedance of free space, respectively. In an equivalent circuit, Z_{in} can be written as

$$Z_{in} = Z_{p1} \parallel Z_{p2} \parallel Z_{p3} \parallel Z_{in1} \tag{6}$$

Z_{p1}, Z_{p2}, and Z_{p3} represent the impedances of the three parallel RLC circuits, and Z_{in1} represents the impedance of the short-circuit transmission line. The values of these impedances can be interpreted in this way:

$$Z_{pj} = R_j j\omega L_j + 1/(j\omega C_j) \ j = 1, 2, 3, \tag{7}$$

$$Z_{in1} = jZ_d \tan\left(\omega t \sqrt{\varepsilon_d}/c\right) \tag{8}$$

where $Z_d = Z_0/\sqrt{\varepsilon_d}$ is the characteristic impedance of the dielectric substrate and c is the speed of light. In addition, using quasi-static analysis, the equivalent inductance L_j and the equivalent capacitance C_j correspond to the length of the metal strip and the gap between adjacent cells, respectively.

In order to further reveal the physical mechanism of perfect absorption by absorbers, we studied the electric field distribution at the frequency of incident light $f_I = 6.46$ THz, $f_{II} = 7.49$ THz, $f_{III} = 8.53$ THz, and $f_{IV} = 9.45$ THz. Figure 4a, b, c, and d shows top views of the electric field distribution near graphene. The electric field at f_I is concentrated at the two vertices at the bottom of the upper and lower triangles, and f_{II} is the result of almost all triangle vertices acting together. The electric field strength at f_{III}

Fig. 3 The ECM of the designed MA.

is limited to the top of the bottom edges of the left and right triangles, and the electric field at the top of the bottom edges of the upper and lower triangles makes a small impurity peak in the absorption peak of f_{III}. The resonance peak of f_{IV} is the result of the electric field at all the vertices of the upper and lower triangles. The four absorption peaks are mainly caused by the coupling between the vibration frequency of the graphene layer and the wavelength of the incident light, and the electric dipole resonance between the triangular pattern and the "X" pattern consumes the energy of the incident light, thus achieving perfect absorption.

In the actual work process, the incident wave is not only vertical, and the absorber must perform well under the condition of oblique incidence. Therefore, we studied the absorption of the absorber at a wide range of incident angles in the simulation process. First, we tested the absorption of MA at different polarization angles at perpendicular incidence, and as can be seen in Fig. 5, the absorption curves of MA are in perfect agreement with each other in the range of 0°–80° polarization. This indicates that the polarization angle has no effect on the absorption of the device, because the structure of the MA is highly symmetrical. As shown in Fig. 6a, the incident angle θ of the light source under the transverse electric (TE) mode polarization condition in the range of 0°–70°, the resonance wavelength is almost unchanged. As shown in Fig. 6b, under the transverse magnetic (TM) mode polarization condition, the absorber will hardly change with the increase of the incident angle, and when the incident angle at $\theta > 50°$, the four absorption peaks have a slight blueshift. This is because, under the TM polarization condition, the dielectric constant of the waveguide layer of the absorber decreases with the increase of the incident angle. In addition, under the polarization conditions of TE and TM, the absorption of the absorber can achieve more than 99% absorption effect at the incidence angle $\theta \leq 50°$, and even when the incidence angle θ is 60°, the absorption effect of the four absorption peaks can achieve 90% and 94%. This proves that the multi-band perfect absorber of the single-layer graphene designed by us is not sensitive to angle, and in practical applications, we can design a matrix with a certain inclination angle so that the absorber attaches to its surface to increase the absorption effect, which provides more possibilities for the device.

The absorption effect of the absorber can be adjusted by changing the graphene pattern and structural parameters, but once the structure is fixed, it is difficult for us to change these parameters. However, due to the dynamic adjustability of graphene, we can flexibly manipulate absorption by adjusting the Fermi level and relaxation rate of graphene. Figure 7 shows the effect of the Fermi level on multi-band absorption performance. It can be seen from the figure that when the Fermi level increases from 0.7 eV to 1.0 eV, the absorption intensity
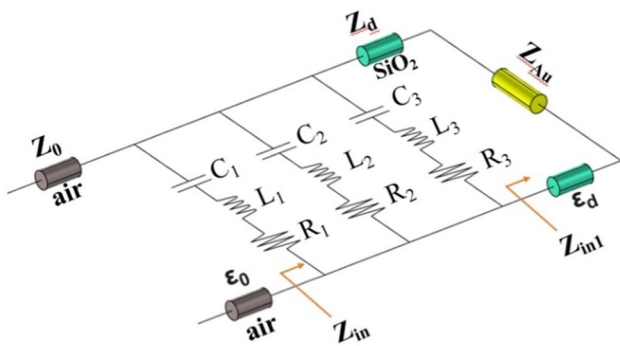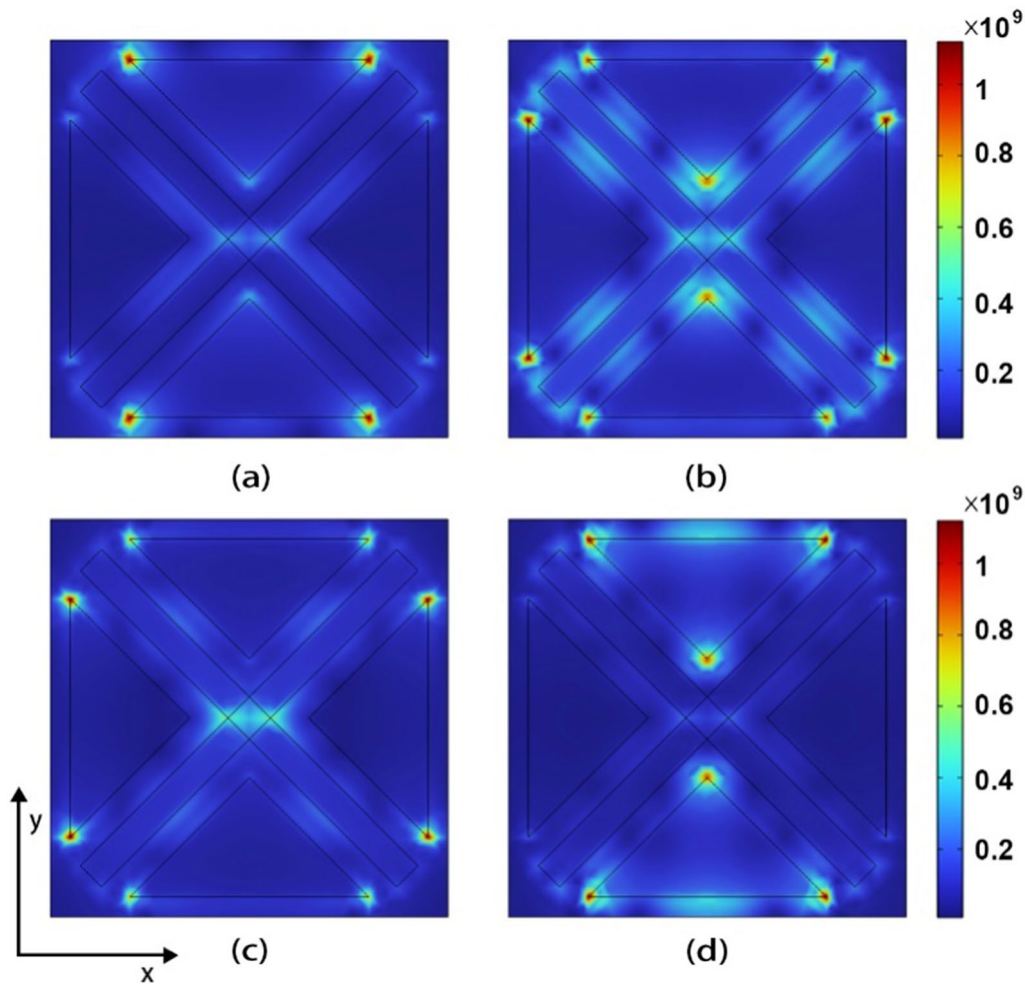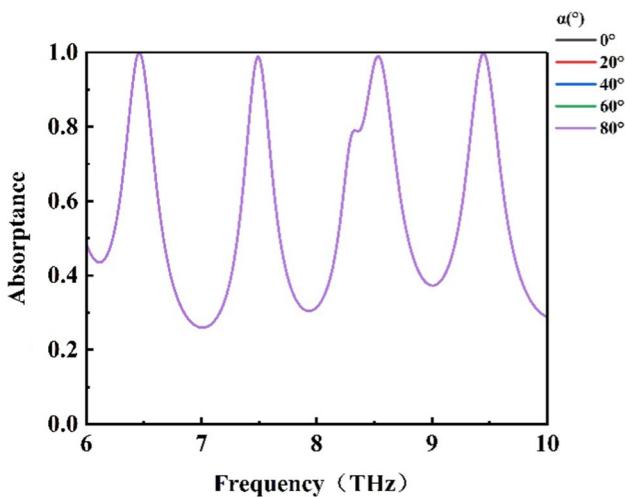
Fig. 4 (a)–(d) The distribution of the transverse interface electric field on the MA surface in the x–y direction when the frequencies of incident light are $f_I = 6.46$ THz, $f_{II} = 7.49$ THz, $f_{III} = 8.53$ THz, and $f_{IV} = 9.45$ THz, respectively.


Fig. 5 Absorption spectra of MA at different polarization angles.

increases continuously and a significant blue shift occurs. This phenomenon can be explained by resonance conditions.[44,45] The formula is as follows:

$$\lambda_\gamma \propto \sqrt{2\pi^2 \hbar c L / \left(\alpha_0 E_F\right)} \tag{9}$$

where λ_γ is the resonant wavelength, L is the graphene nanoribbon length, and $\alpha_0 = e^2/(\hbar c)$ is the coefficient related to the geometry of the model. It can be seen from this equation that with the increase of E_F, the resonance wavelength λ_γ decreases, and the blue shift phenomenon occurs. This also shows that when the geometric parameters of the absorber are fixed, we can adjust the absorption of the absorber by changing the Fermi level.

Next is the effect of relaxation rate on multi-band absorption performance. As can be seen from Fig. 8, as the relaxation rate increases from 0.5 ps to 0.9 ps, the peak value of the absorption peak of f_{III} increases, and the peak of the absorption peak at the other three resonant frequencies increases.
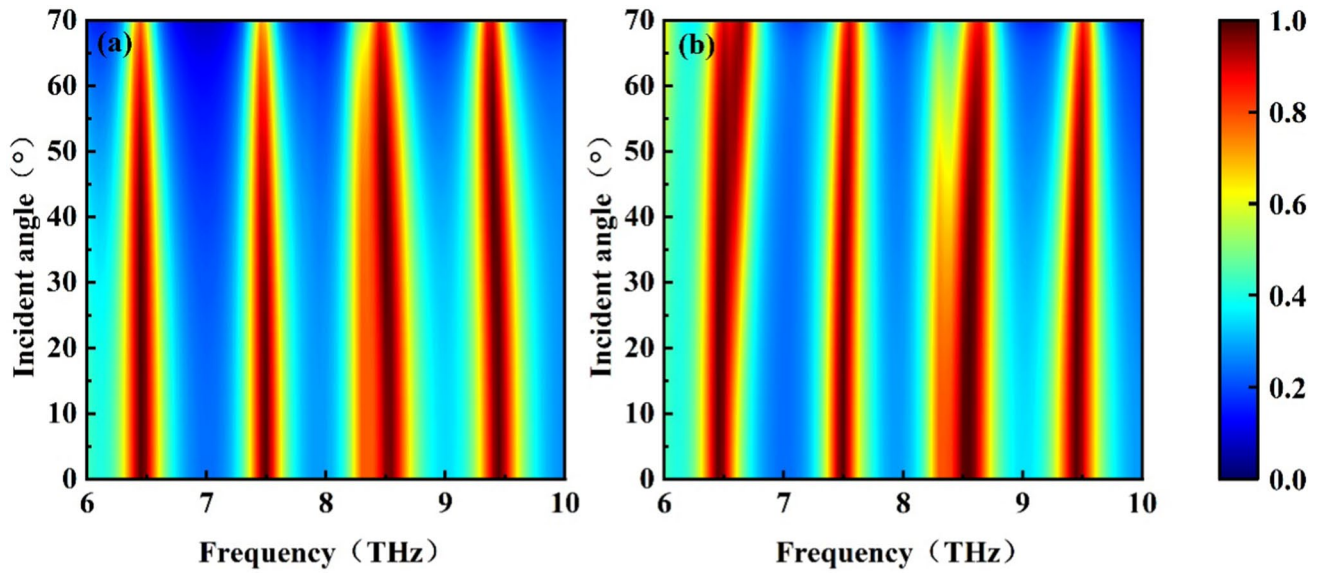
Fig. 6 Under TE polarization (a) and TM polarization (b) conditions, the absorption spectrum of the light source incidence angle increases from 0° to 70°.
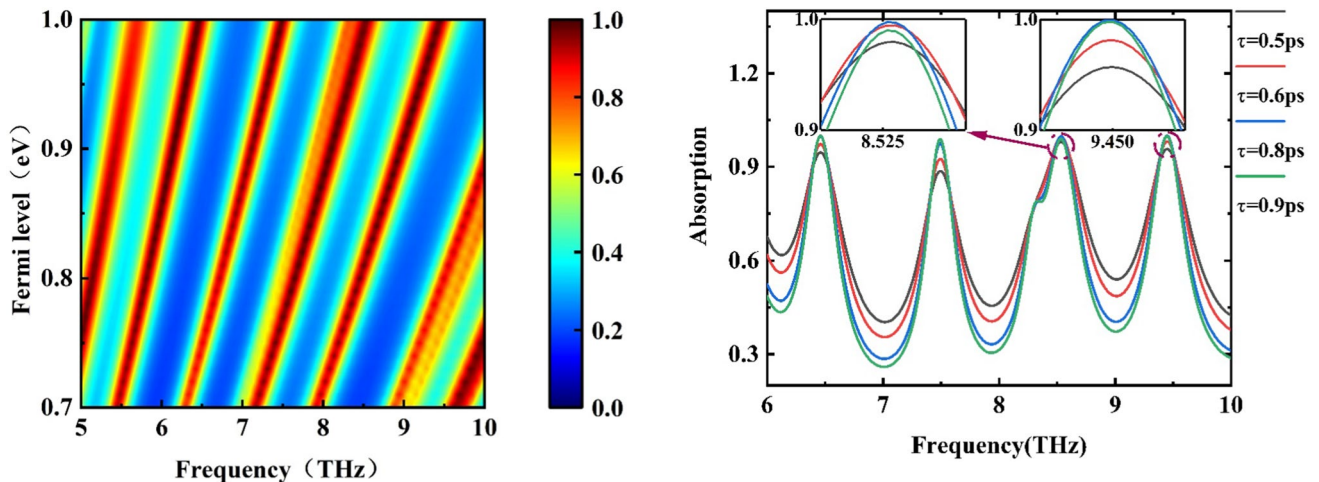
Fig. 7 Absorption spectrum obtained when the geometry of the MA is fixed, and only the Fermi energy level of graphene is increased from 0.7 eV to 1.0 eV.

Fig. 8 The resulting absorption spectrum when the geometry of the MA is fixed, and only the relaxation rate of graphene is increased from 0.5 ps to 0.9 ps.

The reason for this phenomenon is that the increase in relaxation rate will improve the effect of carriers on plasma oscillations, but at certain frequencies, if the relaxation rate is large enough, it will cause the carriers to be saturated, the energy will be reflected, and the peak of the absorption will be reduced.[46,47]

Considering that the strength of the applied magnetic field also has an effect on the conductivity of graphene, we studied the absorption of MA under different applied magnetic field strengths. As shown in Fig. 9, it can be seen that as the magnetic field strength increases, the frequency

corresponding to the absorption peak shifts to the high frequency, and a blue shift occurs. When we apply a magnetic field perpendicular to the surface of graphene, the conductivity of graphene becomes in the form of tensor, the expression of which is[55,56]:

$$\sigma = \begin{pmatrix} \sigma_{xx} & \sigma_{xy} & 0 \\ \sigma_{yx} & \sigma_{yy} & 0 \\ 0 & 0 & \sigma_{zz} \end{pmatrix} \tag{10}$$

Each component can be expressed as
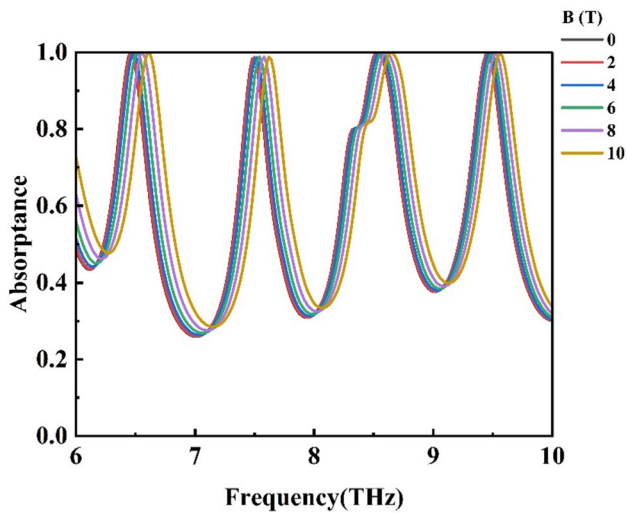
Fig. 9 Absorption curves of MA at different applied magnetic field strengths.

$$\sigma_{xx}(\omega, B) = \sigma_{yy}(\omega, B) = \frac{e^2|E_f|}{\pi\hbar^2} \frac{i(\omega + i/\tau)}{(\omega + i/\tau)^2 - \omega_c^2} \quad (11)$$

$$\sigma_{xy}(\omega, B) = -\sigma_{yx}(\omega, B) = \frac{e^2|E_f|}{\pi\hbar^2} \frac{\omega_c}{(\omega + i/\tau)^2 - \omega_c^2} \quad (12)$$

$$\sigma_{zz}(\omega) = \frac{e^2|E_f|}{\pi\hbar^2} \frac{i}{(\omega + i/\tau)} \quad (13)$$

$\tau = 1/\Gamma$ in the formula is the relaxation time and $\omega_c = eBV_f^2/E_f$ is the electron rotation frequency of graphene. From the above component formula, we can see that the conductivity component of graphene σ_{zz} is independent of the magnetic field, so when the applied magnetic field strength is zero, the conductivity tensor will become a matrix with equal diagonal elements and zero diagonal elements, that is, graphene is an isotropic medium at this time. When the applied magnetic field strength is non-zero, the conductivity becomes anisotropic, which can cause the plasmon on the surface of graphene to propagate in different directions. Therefore, we can control the dynamic control of the device by controlling the strength of the applied magnetic field.

We further investigate how structural parameters and the size of geometric patterns affect multi-band absorption. In this study, we consistently maintained a Fermi level and relaxation rate of 1.0 eV and 0.9 ps, respectively. First, we studied the relationship between the absorption performance of the absorber and the thickness of the dielectric layer, as shown in Fig. 10a. When the pattern parameters were fixed, the absorption peak underwent a significant redshift when the dielectric layer increased from 3.7 μm to 4.0 μm, and the absorption peak-to-peak of f_{II} gradually increased with the increase of the thickness of the dielectric layer, from 96.86% to 99.60%. This can be explained using the interference theory. Part of the incident wave is reflected directly by the graphene on the surface of the absorber, and the rest is transmitted to the dielectric layer, where it is reflected several times and then propagated to the top surface again. The dielectric layer plays an important role as a Fabry–Perot resonator during absorption,[48,49] and its thickness leads to constructive/destructive interference and further modulates the absorption spectrum.

Next, we investigate the influence of the geometric parameters of the pattern on the performance of the absorber, as shown in Fig. 10b. Under the premise of fixing other parameters, when the length of the bottom edge of the triangle pattern changed from 2.2 μm to 2.5 μm, f_I and f_{III} remained relatively stable, f_{II} underwent obvious redshift, and f_{IV} showed first a blue shift and then a red shift. This is because when the distance between the triangle and the X figure is close, f_I and f_{II}, f_{III}, and f_{IV} interact, and once the distance reaches the critical limit, the original resonant mode is destroyed and a new resonant mode is excited.[50]

Finally, we investigated the sensing performance of MA in detecting changes in the refractive index of some specific analytes. We replace the air medium covered with the MA with the analyte to be detected. The refractive index of these substances ranges from 1.33 to 1.5, which includes water (refractive index 1.33), ethanol (refractive index 1.36), ethylene glycol (refractive index 1.41), cyclohexane (refractive index 1.45), and benzene (refractive index 1.5). As shown in Fig. 11a, at room temperature, as the refractive index of the different analytes increases, the four absorption peaks are significantly redshifted. Except for a slight decrease in the f_{II} absorption peak, the absorption efficiency of the absorption peaks remained almost unchanged. This indicates that analytes with different refractive indices can be resolved by shifting the resonant frequency of the absorption peak due to a change in the refractive index. To further investigate the sensor performance of MA, sensitivity (*S*) and the figure of merit (FOM) are two parameters commonly used to evaluate device performance. Defined as[51-53]
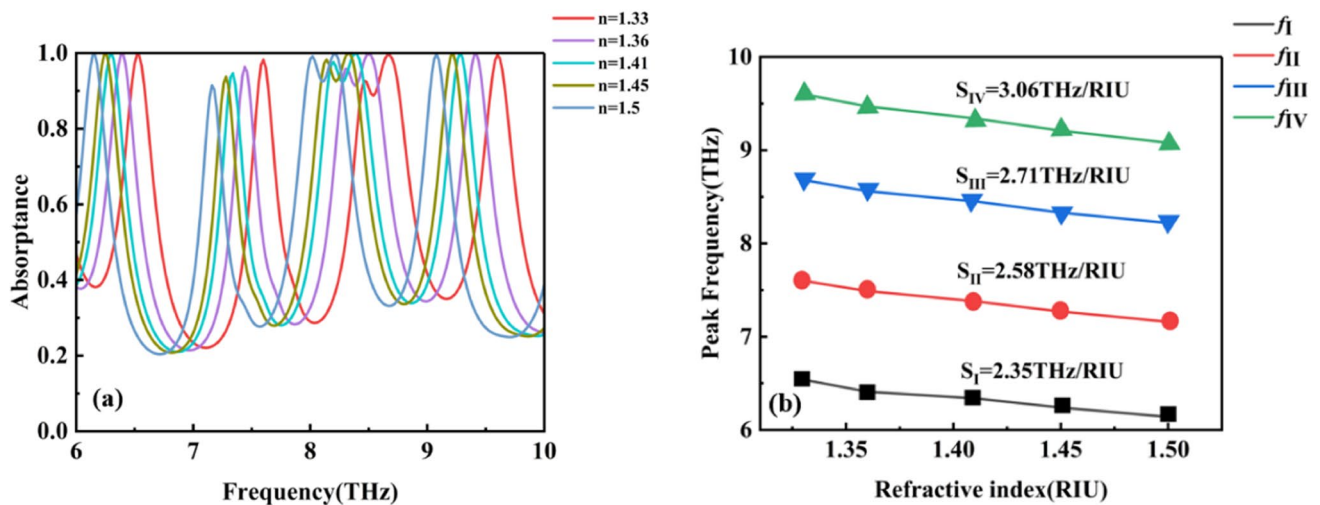
$$S = \frac{\Delta f}{\Delta n} \quad (14)$$

$$\text{FOM} = \max\left(\left|\frac{\Delta A}{A * \Delta n}\right|\right) \quad (15)$$
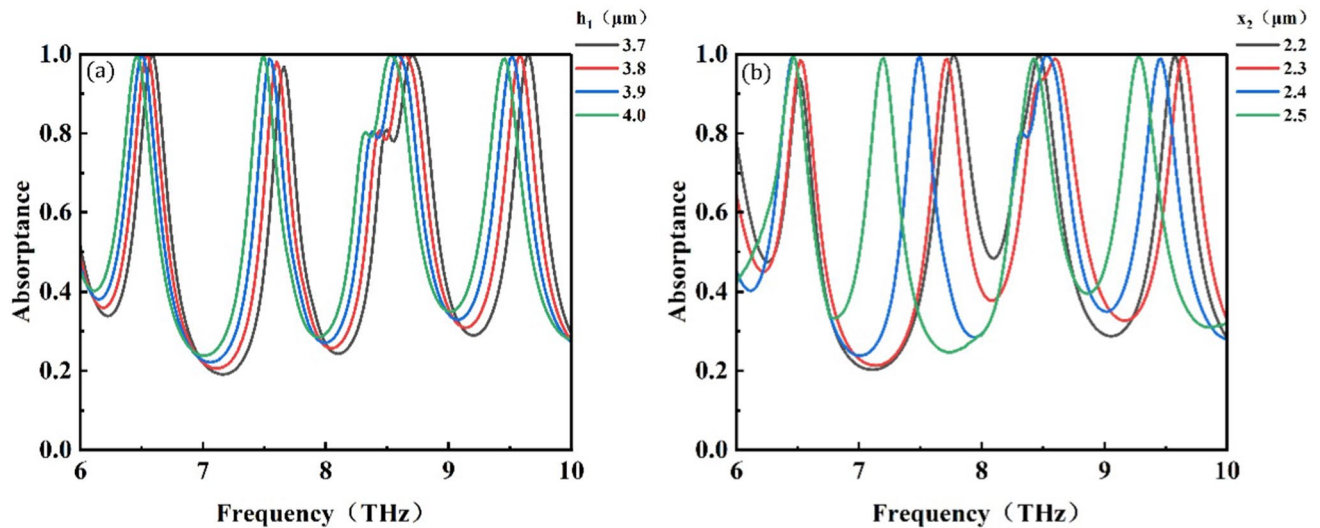
Fig. 10 When other parameters remain unchanged, (a) the absorption spectrum obtained when the thickness of the dielectric layer h_1 of MA increases from 3.7 μm to 4.0 μm; (b) the corresponding absorption spectrum obtained when the length x_2 of the base side of the triangle is increased from 2.2 μm to 2.5 μm.

Fig. 11 (a) Absorption spectra of MA at different refractive indices. (b) The resonance frequency is linearly related to the refractive index.

S represents the frequency shift of the refractive index unit (RIU) change. $\frac{\Delta A}{\Delta n}$ represents the change in relative peak absorptivity caused by the change in refractive index Δn.

As shown in Fig. 11b, the sensitivities of the four absorption peaks are $S_{\mathrm{I}} = 2.35$ THz/RIU, $S_{\mathrm{II}} = 2.58$ THz/RIU, $S_{\mathrm{III}} = 2.71$ THz/RIU, and $S_{\mathrm{IV}} = 3.06$ THz/RIU, respectively. In addition, the calculation shows that the maximum FOM value can reach 54.6.

Finally, we compared the proposed MA with some of the reported devices, as shown in Table I. The results show that the device we designed not only has multiple absorption bands, but also has better sensing performance. This

provides a more valuable reference for further design and research of graphene-based MAs.

Conclusion

In summary, this paper describes the design and study of a multi-band perfect absorber based on a single layer of graphene, which is composed of a single-layer patterned graphene, a silica dielectric layer, and a gold substrate, which has the characteristics of simple structure. Using the COMSOL commercial software, it is confirmed that the absorber has absorption peaks of 99.99%, 99.60%, 99.87%,

Table I Comparison of this absorber with similar single-layer graphene absorbers

References	Number of absorption bands	Max sensitivity (THz/RIU)	FOM
Ref. 54	3	1.6	26.4
Ref. 20	2	2.34	28.3
Ref. 53	4	2.97	47.5
Work	4	3.06	54.6

and 99.00% at $f_I = 6.46$ THz, $f_{II} = 7.49$ THz, $f_{III} = 8.53$ THz, and $f_{IV} = 9.45$ THz, respectively, and can maintain absorption of more than 90% at a wide range of incidence angles of 0°–70°. At the same time, we proved the multi-band perfect absorption principle of the device through the ECM and internal electric field analysis. In addition, the optical properties of the absorption spectrum are further revealed by changing the thickness of the dielectric layer and changing the size of the graphene pattern. In addition, by adjusting the strength of the applied magnetic field, the Fermi level, and the relaxation rate of graphene, the resonance wavelength and absorption efficiency of the absorber can be dynamically adjusted. Finally, the sensing performance of the absorber was investigated by varying the analytes overlaid on the device, with the highest S and FOM of 3.06 THz/RIU and 54.6 for the absorber. Therefore, the device has broad application prospects in photoelectric sensing and chemical detection, and also provides an important reference value for the research in this field.

References

1. Z. Zheng, Y. Zheng, Y. Luo, Z. Yi, J. Zhang, L. Liu, Q. Song, P. Wu, Y. Yu, and J. Zhang, Terahertz perfect absorber based on flexible active switching of ultra-broadband and ultra-narrowband. *Opt. Express* 29, 42787 (2021).

2. R. Nie, C. He, R. Zhang, and Z. Song, Vanadium dioxide-based terahertz metasurfaces for manipulating wavefronts with switchable polarization. *Opt. Laser Technol.* 159, 109010 (2023).

3. W.L. Barnes, A. Dereux, and T.W. Ebbesen, Surface plasmon subwavelength optics. *Nature* 424, 6950 (2003).

4. D.R. Smith, W.J. Padilla, D. Vier, S.C. Nemat-Nasser, and S. Schultz, Composite medium with simultaneously negative permeability and permittivity. *Phys. Rev. Lett.* 84, 4184 (2000).

5. B. Spackova, P. Wrobel, M. Bockova, and J. Homola, Optical biosensors based on plasmonic nanostructures: a review. *Proc. IEEE* 104, 2380–2408 (2016).

6. J. Valentine, S. Zhang, T. Zentgraf, E. Ulin-Avila, D.A. Genov, G. Bartal, and X. Zhang, Three-dimensional optical metamaterial with a negative refractive index. *Nature* 455, 7211 (2008).

7. L. Ye, X. Chen, G. Cai, J. Zhu, N. Liu, and Q.H. Liu, Electrically tunable broadband terahertz absorption with hybrid-patterned graphene metasurfaces. *Nanomater-Basel* 8, 562 (2018).

8. Z. Zhou, Y. Chen, Y. Tian, J. Liang, and W. Yang, Ultra-broadband metamaterial perfect solar absorber with polarization-independent and large incident angle-insensitive. *Opt. Laser Technol.* 156, 108591 (2022).

9. Y. Cheng, R. Gong, and J. Zhao, A photoexcited switchable perfect metamaterial absorber/reflector with polarization-independent and wide-angle for terahertz waves. *Opt. Mater.* 62, 28 (2016).

10. S. Zhang, D.A. Genov, Y. Wang, M. Liu, and X. Zhang, Plasmon-induced transparency in metamaterials. *Phys. Rev. Lett.* 101, 047401 (2008).

11. Z. Song, Q. Chu, and Q.H. Liu, Isotropic wide-angle analog of electromagnetically induced transparency in a terahertz metasurface. *Mater. Lett.* 223, 90 (2018).

12. Z. Zheng, Y. Luo, H. Yang, Z. Yi, J. Zhang, Q. Song, W. Yang, C. Liu, X. Wu, and P. Wu, Thermal tuning of terahertz metamaterial absorber properties based on VO$_2$. *Phys. Chem. Chem. Phys.* 24, 8846 (2022).

13. A. Fardoost, F.G. Vanani, A.A. Amirhosseini, and R. Safian, Design of a multilayer graphene-based ultrawideband terahertz absorber. *IEEE T. Nanotechnol.* 16, 68 (2016).

14. Y. Cai, J. Zhu, and Q.H. Liu, Tunable enhanced optical absorption of graphene using plasmonic perfect absorbers. *Appl. Phys. Lett.* 106, 043105 (2015).

15. Z. Li, S. Butun, and K. Aydin, Large-Area, lithography-free super absorbers and color filters at visible frequencies using ultrathin metallic films. *ACS Photonics* 2, 183 (2015).

16. F. He, B. Han, X. Li, T. Lang, X. Jing, and Z. Hong, Analogue of electromagnetically induced transparency with high-Q factor in metal-dielectric metamaterials based on bright-bright mode coupling. *Opt. Express* 27, 37590 (2019).

17. N.I. Landy, S. Sajuyigbe, J.J. Mock, D.R. Smith, and W.J. Padilla, Perfect metamaterial absorber. *Phys. Rev. Lett.* 100, 207402 (2008).

18. H. Chen, Z. Chen, H. Yang, L. Wen, Z. Yi, Z. Zhou, B. Dai, J. Zhang, X. Wu, and P. Wu, Multi-mode surface plasmon resonance absorber based on dart-type single-layer graphene. *RSC Adv.* 12, 7821 (2022).

19. F. Qin, X. Chen, Z. Yi, W. Yao, H. Yang, Y. Tang, Y. Yi, H. Li, and Y. Yi, Ultra-broadband and wide-angle perfect solar absorber based on TiN nanodisk and Ti thin film structure. *Sol. Energ. Mat. Sol. C.* 211, 110535 (2020).

20. K.T. Lin, H. Lin, T. Yang, and B. Jia, Structured graphene metamaterial selective absorbers for high efficiency and omnidirectional solar thermal energy conversion. *Nat. commun.* 11, 1389 (2020).

21. K.S. Novoselov, A.K. Geim, S.V. Morozov, D. Jiang, Y. Zhang, S.V. Dubonos, I.V. Grigorieva, and A.A. Firsov, Electric field effect in atomically thin carbon films. *Science* 306, 666 (2004).

22. S. Bae, H. Kim, Y. Lee, X. Xu, J.S. Park, Y. Zheng, J. Balakrishnan, T. Lei, H. Ri Kim, and Y. Song, Roll-to-roll production of 30-inch graphene films for transparent electrodes. *Nat. Nanotechnol.* 5, 574 (2010).

23. K.F. Mak, M.Y. Sfeir, Y. Wu, C.H. Lui, J.A. Misewich, and T.F. Heinz, Measurement of the optical conductivity of graphene. *Phys. Rev. Lett.* 101, 196405 (2008).

24. M.D. Kapetanakis, W. Zhou, M.P. Oxley, J. Lee, M.P. Prange, S.J. Pennycook, J.C. Idrobo, and S.T. Pantelides, Low-loss electron energy loss spectroscopy: an atomic-resolution complement to optical spectroscopies and application to graphene. *Phys. Rev. B* 92, 125147 (2015).

25. M. Islam, J. Sultana, M. Biabanifard, Z. Vafapour, M. Nine, A. Dinovitser, C. Cordeiro, B.H. Ng, and D. Abbott, Tunable localized surface plasmon graphene metasurface for multiband superabsorption and terahertz sensing. *Carbon* 158, 559 (2020).

26. S. Thongrattanasiri, F.H. Koppens, and F.J.G. De Abajo, Complete optical absorption in periodically patterned graphene. *Phys. Rev. Lett.* 108, 047401 (2012).

27. G. Yao, F. Ling, J. Yue, C. Luo, J. Ji, and J. Yao, Complete optical absorption in periodically patterned graphene. *Opt. Express* 24, 1518 (2016).

28. X. Luo, Z.Q. Cheng, X. Zhai, Z.M. Liu, S.Q. Li, J.P. Liu, L.L. Wang, Q. Lin, and Y.H. Zhou, A tunable dual-band and polarization-insensitive coherent perfect absorber based on double-layers graphene hybrid waveguide. *Nano Express* 14, 1 (2019).

29. W. Yin, Z. Shen, S. Li, L. Zhang, and X. Chen, A three-dimensional dual-band terahertz perfect absorber as a highly sensitive sensor. *Front. Phys-Lausanne* 9, 665280 (2021).

30. Z. Liu, S. Zhuo, F. Zhou, X. Zhang, Y. Qin, X. Luo, C. Ji, and G. Yang, Double narrowband induced perfect absorption photonic sensor based on graphene–dielectric–gold hybrid metamaterial. *Nanoscale Res. Lett.* 17, 85 (2022).

31. M. Liu, X. Yin, and X. Zhang, Double-layer graphene optical modulator. *Nano Lett.* 12, 1482 (2012).

32. C.H. Gan, H.S. Chu, and E.P. Li, Synthesis of highly confined surface plasmon modes with doped graphene sheets in the midinfrared and terahertz frequencies. *Phys. Rev. B* 85, 125431 (2012).

33. W. Zhu, I.D. Rukhlenko, F. Xiao, C. He, J. Geng, X. Liang, M. Premaratne, and R. Jin, Multiband coherent perfect absorption in a water-based metasurface. *Opt. Express* 25, 15737 (2017).

34. F. Liu, M. He, Z. Dong, Y. Wang, and B. Ni, Design of tunable dual-band terahertz perfect absorber base on graphene. *Results Phys.* 40, 105860 (2022).

35. P. Zamzam, P. Rezaei, and S.A. Khatami, Quad-band polarization-insensitive metamaterial perfect absorber based on bilayer graphene metasurface. *Phys. E* 128, 114621 (2021).

36. Y. Cai, Y. Guo, H. Zhang, Y. Wang, C. Chen, F. Lin, S. Zuo, and Y. Zhou, Tunable and polarization-sensitive graphene-based terahertz absorber with eight absorption bands. *J. Phys. D Appl. Phys.* 54, 195106 (2021).

37. M. Liu, H.Y. Hwang, H. Tao, A.C. Strikwerda, K. Fan, G.R. Keiser, A.J. Sternbach, K.G. West, S. Kittiwatanakul, and J. Lu, Terahertz-field-induced insulator-to-metal transition in vanadium dioxide metamaterial. *Nature* 487, 345 (2012).

38. Z. Song, Y. Deng, Y. Zhou, and Z. Liu, Terahertz toroidal metamaterial with tunable properties. *Opt. Express* 27, 5792 (2019).

39. Y. Liu, M. Bo, X. Yang, P. Zhang, C.Q. Sun, and Y.J. Huang, Size modulation electronic and optical properties of phosphorene nanoribbons: DFT–BOLS approximation. *Phys. Chem. Chem. Phys.* 19, 5304 (2017).

40. W. Wei, J. Wu, S. Cui, Y. Zhao, W. Chen, and L. Mi, α-Ni $(OH)_2$/NiS$_{1.97}$ heterojunction composites with excellent ion and electron transport properties for advanced supercapacitors. *Nanoscale* 11, 6243 (2019).

41. G. Li, T. Sang, H. Qi, X. Wang, X. Yin, Y. Wang, and L. Hu, Flexible control of absorption enhancement of circularly polarized light via square graphene disks. *OSA Continuum.* 3, 1999 (2020).

42. Y. Li, M. Li, P. Xu, S. Tang, and C. Liu, Efficient photocatalytic degradation of acid orange 7 over N-doped ordered mesoporous titania on carbon fibers under visible-light irradiation based on three synergistic effects. *Appl. Catal. A-Gen.* 524, 163 (2016).

43. X. Zeng, M. Gao, L. Zhang, G. Wan, and B. Hu, Design of a triple-band metamaterial absorber using equivalent circuit model and interference theory. *Microw. Opt. Techn. Let.* 60, 1676 (2018).

44. H. Cheng, S. Chen, P. Yu, X. Duan, B. Xie, and J. Tian, Dynamically tunable plasmonically induced transparency in periodically patterned graphene nanostrips. *Appl. Phys. Lett.* 103, 203112 (2013).

45. F.H. Koppens, D.E. Chang, and F.J. Garcia de Abajo, Graphene plasmonics: a platform for strong light–matter interactions. *Nano Lett.* 11, 3370 (2011).

46. A. Bhattacharya, K.M. Devi, T. Nguyen, and G. Kumar, Actively tunable toroidal excitations in graphene based terahertz metamaterials. *Opt. Commun.* 459, 124919 (2020).

47. J. Li, X. Chen, Z. Yi, H. Yang, Y. Tang, Y. Yi, W. Yao, J. Wang, and Y. Yi, Broadband solar energy absorber based on monolayer molybdenum disulfide using tungsten elliptical arrays. *Mater. Today Energy* 16, 100390 (2020).

48. Z.D. Yan, X. Lu, W. Du, Z. Lv, C. Tang, P. Cai, P. Gu, J. Chen, and Z. Yu, Ultraviolet graphene ultranarrow absorption engineered by lattice plasmon resonance. *Nanotechnology* 32, 465202 (2021).

49. M. Vaughan, *The Fabry-Perot interferometer: history, theory, practice and applications* (Milton Park: Routledge, 2017).

50. H.T. Chen, Interference theory of metamaterial perfect absorbers. *Opt. Express* 20, 7165 (2012).

51. B. Jan, T. Andreas, J. Arpad, H. Ulrich, and S. Carsten, The optimal aspect ratio of gold nanorods for plasmonic bio-sensing. *Plasmonics* 5, 161 (2010).

52. W. Wang, K.J. Wang, Z.G. Yang, and J.S. Liu, Experimental demonstration of an ultra-flexible metamaterial absorber and its application in sensing. *J. Phys. D Appl. Phys.* 13, 135108 (2017).

53. J.P. Tian, R.J. Ke, R.C. Yang, and W.H. Pei, Tunable quad-band perfect metamaterial absorber on the basis of monolayer graphene pattern and its sensing application. *Results Phys.* 26, 104447 (2021).

54. B.X. Wang, G.Z. Wang, and T. Sang, Simple design of novel triple-band terahertz metamaterial absorber for sensing application. *J. Phys. D Appl. Phys.* 49, 165307 (2016).

55. R. Cheng, Y. Zhou, H. Liu, J. Liu, G. Sun, X. Zhou, H. Shen, Q. Wang, and Y. Zha, Tunable graphene-based terahertz absorber via an external magnetic field. *Opt. Mater. Express* 10, 501 (2020).

56. H.F. Liu, J.X. Wu, J.R. Yuan, and X.H. Deng, Dynamically tunable perfect THz absorption in graphene-based metamaterial structures. *Europhys. Lett.* 134, 57003 (2021).